Journal of Catalysis 453 (2026) 116464

Contents lists available at ScienceDirect

Journal of Catalysis

journal homepage: www.elsevier.com/locate/jcat

Research article

# Synergistic acid–base interplays: Zeolite-catalyzed $CH_3Cl$ conversion to light olefins boosted by MgO-driven $CH_3Cl$ spillover

Seungdon Kwon [1], Jun Hyeok Heo [1], Changgi Kim, Woosung Leem, Hanbit Jang, Kyungsu Na [*]

*Department of Chemistry, Chonnam National University, Gwangju 61186, Republic of Korea*

ARTICLE INFO

*Keywords:*
Chloromethane–to–olefin
Zeolite catalyst
C1 conversion
Light olefin
$CH_3Cl$ spillover
Balanced catalytic interplay

ABSTRACT

Chloromethane ($CH_3Cl$), a reactive $C_1$ molecule, has been underexplored compared to traditional $C_1$ molecules like CO, $CO_2$, $CH_4$, and $CH_3OH$ that have long been at the center of $C_1$ chemistry. Herein, the catalytic chloromethane–to–olefin (CMTO) reaction was investigated with zeolite-based heterogeneous acid catalysts. H-ZSM-5 zeolites with controlled Si/Al ratios were investigated, revealing that $CH_3Cl$ conversion, catalyst lifetime, and light olefin ($C_{2-4}^{=}$) selectivity depended on zeolite acidity and MgO addition. While MgO alone enabled $CH_3Cl$ activation via Lewis acid–base interactions, its independent catalytic play pales compared to the superior performance of zeolites. However, balancing the zeolite acidity with MgO loading doubled or even tripled $CH_3Cl$ conversion compared to the independent performance of zeolites, achieving nearly 100 % $CH_3Cl$ conversion with 86.5 % $C_{2-4}^{=}$ selectivity without deactivation. In-situ diffuse reflectance infrared Fourier transform spectroscopy showed that both zeolite acid sites and MgO activated $CH_3Cl$ simultaneously, during which MgO induced a $CH_3Cl$ spillover to the zeolite acidic site, resulting in the boosted $CH_3Cl$ conversion. This study establishes a new road to efficient and selective $C_1$ molecular conversion using $CH_3Cl$ boosted by $CH_3Cl$ spillover, which would be extended to methyl spillover-mediated catalytic conversion to various chemicals.

## 1. Introduction

Light olefins ($C_{2-4}^{=}$) including ethylene, propylene, and butylene are essential building blocks for synthesizing a wide range of chemical products [1]. In modern chemical industries, light olefins are typically produced via key processes such as steam cracking, fluid catalytic cracking (FCC), and dehydrogenation. These methods are primarily petroleum-based top-down approaches that often generate various undesirable carbonaceous byproducts, including $C_1$-based small molecules such as $CO_2$, CO and $CH_4$, which contribute to greenhouse gas emissions [1]. Both steam cracking and dehydrogenation are highly energy-intensive processes, requiring extremely high reaction temperatures that result in significant $CO_2$ emissions and high operational costs [1–5]. While FCC is being widely used, it primarily produces gasoline with lower propylene yields and is challenged by issues like catalyst contamination, necessitating frequent replacements [5]. In contrast, the methanol–to–olefin (MTO) process represents a bottom-up approach that activates methanol ($CH_3OH$) to produce light olefins. This process requires zeolite catalysts and a stable methanol supply, typically via steam methane reforming (SMR) [1,6–9]. With rapidly rising crude oil prices and the steady depletion of fossil fuel reserves, traditional petroleum-based methods cannot meet the growing demand for light olefins, especially in the context of current energy shortages [1,4,8–10].

A two-step process for converting $CH_4$ to light olefins via chloromethane ($CH_3Cl$) as an intermediate is emerging as a promising, sustainable alternative for efficient light olefin production in the chemical industry [6,11–15]. In the first step, $CH_4$ undergoes oxychlorination [11,16,17] or chlorination [18–23] to produce $CH_3Cl$, achieving high $CH_3Cl$ selectivity over 90 % through the selective monochlorination of $CH_4$ using an acidic catalyst [21–23] Subsequently, $CH_3Cl$ can be converted to olefins in the chloromethane–to–olefins (CMTO) process using zeolite-based acidic catalysts, [12–15,24–37] which parallels the MTO process but substitutes $CH_3OH$ with $CH_3Cl$. The CMTO has gained significant research attention from both academia and industry due to its efficiency in forming C–C bonds from $CH_3Cl$ derived from energy-efficient $CH_4$ chlorination [6,12,13,24]. A major advantage of the

* Corresponding author.
*E-mail address:* kyungsu_na@chonnam.ac.kr (K. Na).
[1] These authors contributed equally to this work.

https://doi.org/10.1016/j.jcat.2025.116464
Received 22 March 2025; Received in revised form 16 September 2025; Accepted 29 September 2025
Available online 6 October 2025

CMTO process is its lower operational costs due to lower reaction temperatures [6,12–15,25–37]. It achieves high olefin yields with excellent selectivity, resulting in minimal byproducts and simpler separation requirements [12–15,25–37]. Additionally, HCl produced as a byproduct during the CMTO reaction can be recycled for reuse in the Deacon process or oxyhydrochlorination process, [6,11,16,17,38,39] contributing to the construction of a sustainable chlorine-mediated $CH_4$ utilization cycle.

The reaction mechanism of the CMTO closely resembles that of the MTO process, primarily due to the similar molecular structures and chemical properties of $CH_3OH$ and $CH_3Cl$ [14,25]. Consequently, much of the research on CMTO has drawn inspiration from MTO researches, advancing catalyst preparation, modification, and mechanistic understanding [14,25]. For instance, Corma et al. [40] and Gao et al. [41] found that AEI-type SAPO-18 zeolites yield higher amounts of propylene and butylene, whereas CHA-type SAPO-34 zeolites achieve the highest ethylene yields. Later, Chae et al. reported that AEI-type zeolites produced a higher propylene/ethylene ratio, attributed to the larger cage volumes of the AEI-type structures compared to CHA-type structures under CMTO reaction conditions [26]. This aligns with the well-established impact of shape selectivity based on hydrocarbon pool (HCP) mechanism in MTO research [7,9,42–46]. It was also reported that fast mass transfer rates in hierarchical zeolites enhanced the overall reaction rate while minimizing secondary reactions and coke formation, both of which contribute to extended catalyst lifetime [27]. The introduction of mesopores or hierarchical pores improves reactant access to catalytic sites, thereby enhancing the reactant conversion. Liu et al. [47] demonstrated that hierarchical H-ZSM-5 catalysts achieved higher olefin selectivity and prolonged catalyst lifetime compared to solely microporous, conventional zeolites. Beyond structural optimization, zeolite acidity also plays a crucial role in reaction results. High-temperature steaming has been found to reduce the total acidity and alter the Brønsted/Lewis acid site ratio in H-ZSM-5 catalysts, while generating secondary pores, collectively resulting in increased olefin yields [48].

Despite these advances, many intrinsic challenges persist in the CMTO reaction. For example, the conversion rate of $CH_3Cl$ is typically slower than that of $CH_3OH$ under similar reaction conditions [49]. Castaño et al. and Olsbye et al. observed significantly reduced $CH_3Cl$ conversion compared to $CH_3OH$ over ZSM-5 catalysts [12,28]. This could be attributed to lower proton affinity of $CH_3Cl$ (647 kJ/mol) than that of $CH_3OH$ (754 kJ/mol), leading to slower $CH_3Cl$ adsorption on Brønsted acid sites (BAS) and hence slower $CH_3Cl$ conversion [28,29]. To overcome this limitation and enhance $CH_3Cl$ conversion, higher reaction temperatures and stronger acidic catalysts are required. However, unlike the MTO process, the CMTO reaction generates HCl as a byproduct, which can induce the dealumination of the zeolite framework [29,30,50]. Although stronger acidic catalysts can increase $CH_3Cl$ conversion, they may also accelerate undesired secondary reactions, such as cracking and hydrogen transfer, potentially leading to the excessive conversion of olefins into paraffins and heavier compounds like polycyclic aromatics. This not only increases coke formation but also reduces catalyst lifetime [29,30]. To develop a more reactive, selective, and sustainable CMTO process, extensive research is required to optimize catalysts with finely tuned acidic properties and to deepen our understanding of their impact on the CMTO process.

Table 1 summarizes representative studies on CMTO reactions using zeolite-based catalysts modified with metal salts. Similarly, we also reported $SnO_2$-impregnated SSZ-13 zeolite catalysts for the CMTO reaction, [13] wherein $SnO_2$ nanocrystals modified the acidic properties of SSZ-13 zeolite, enhanced the $CH_3Cl$ affinity, and thereby achieved superior $CH_3Cl$ conversion and light olefin selectivity. This study demonstrated that optimizing the zeolite acidity and increasing $CH_3Cl$ affinity to the catalytic sites are crucial to afford a high $CH_3Cl$ conversion with high $C_{2-4}^{=}$ selectivity. Although the addition of metal salts has been shown to create catalytic synergies, their specific catalytic contributions remain incompletely understood. While we are exploring further to understand the origin of catalytic synergies from the addition of basic metal oxides based on alkaline earth metals, we discovered systematic $CH_3Cl$ activation based on the different basicity of metal oxides during CMTO reaction (Figs. S1 and S2). Inspired by such systematic changes depending on the basicity of metal oxides, we assumed that there should be a certain interaction between $CH_3Cl$ and metal oxides, which may govern the catalysis. Of the tested metal oxides, MgO exhibited the most superior performance, wherein the specific interaction between MgO and $CH_3Cl$ boosted $CH_3Cl$ activation by MgO-mediated $CH_3Cl$ spillover to the catalytic sites (i.e., acid sites in zeolite framework). The specific $CH_3Cl$ spillover with the balanced interplays of zeolite acid sites and MgO boosted CMTO conversion with increasing light olefin selectivity. Herein, we investigated a series of H-ZSM-5 zeolites with varying Si/Al ratios, in the presence of MgO at various loadings for the CMTO reaction, to investigate the roles of different acidity originated from zeolite lattice and different basicity originated from MgO. Through the systematic controlled study, the catalytic roles of MgO-impregnated H-ZSM-5 zeolites in the CMTO reaction were elucidated with comprehensive characterizations, including in-situ diffuse reflectance infrared Fourier transform spectroscopy (DRIFTS).

## 2. Experimental section

Please refer to the "Supplementary Materials" for this section.

## 3. Results and discussion

### 3.1. Characterization of MgO-impregnated zeolite catalysts

The basicity of the series of H-ZSM-5 zeolites (Si/Al ratio = 40,

**Table 1**
Summary of the performances of the catalysts developed in this study and those of representative reported catalysts.

| Catalyst | $CH_3Cl$ Conv. (%) | Selectivity (%) | | | | | | | | | | Ref. |
|---|---|---|---|---|---|---|---|---|---|---|---|---|
| | | $CH_4$ | $C_2^{=}$ | $C_3^{=}$ | $C_4^{=}$ | $C_2^{-}$ | $C_3^{-}$ | $C_4^{-}$ | BTX | $C_{5+}$ | Total Olefin | |
| 1 wt%MgO/H-ZSM-5 (Si/Al = 40) | 99.9 | 1.6 | 28.8 | 29.7 | 9.9 | 0.6 | 8.1 | 9.7 | 6.6 | 5.0 | 68.4 | this work |
| 5 wt%MgO/H-ZSM-5 (Si/Al = 40) | 97.8 | 1.4 | 5.8 | 64.5 | 16.2 | 0 | 0.1 | 4.7 | 0.1 | 7.2 | 86.5 | this work |
| 15SnO2/H-SSZ-13 | 98.1 | 1.8 | 34.5 | 50.3 | 2.3 | $C_2 \sim C_4$ 3.3 | | | – | 7.8 | 87.1 | [13] |
| CoAPSO-34 | 78.8 | 2.4 | 63.1 | 29.7 | – | 1.2 | 3.7 | – | – | – | 92.8 | [25] |
| MgAPSO-34-C1 | 99.7 | 1.4 | 44.7 | 37.0 | 6.4 | 0.2 | 0.9 | 2.2 | – | 5.8 | 88.1 | [15] |
| 7 %Mg-H-ZSM-5 (Si/Al = 25) | 99.0 | 1.1 | 12.2 | 60.3 | 17.8 | 0.1 | 0.1 | 0.1 | – | 4.4 | 90.3 | [36] |
| 5 %Mg-H-ZSM-5 (Si/Al = 40) | 89.8 | – | 8.0 | 65.4 | 17.2 | 0.2 | – | – | – | 5.3 | 90.6 | [37] |
| 5 %Mg-H-ZSM-5 (Si/Al = 15) | 87.5 | – | 3.7 | 59.0 | 21.4 | 0.1 | – | – | – | 7.2 | 84.1 | [37] |
| 0.33 %Mg-APSO-34 | 98.0 | 3.1 | 15.3 | 19.3 | 11.5 | 4.1 | 30.4 | 3.4 | – | 12.9 | 46.1 | [35] |
| Mg-ZSM-5 (Si/Al = 15) | 95.0 | – | 17.2 | 25.1 | 6.8 | – | 12.4 | – | – | – | 49.1 | [32] |
| 5 %MnAPSO−34 | 99.0 | 2.3 | 18.5 | 19.7 | 15.1 | 1.8 | 21.1 | 2.8 | – | 18.7 | 53.3 | [34] |
| $Mn^{2+}$-ZSM-5 (Si/Al = 25) | 99.4 | 0.6 | – | 13.7 | 9.0 | 8.8 | 17.4 | 15.7 | 16.6 | 18.2 | 22.7 | [31] |
| 1.8 %Mn-APSO-34 | 96.5 | – | 41.2 | 30.5 | 8.7 | $C_1 \sim C_4$ 8.4 | | | – | 11.2 | 80.4 | [33] |

denoted as Z40) impregnated with various alkaline earth metal oxides was characterized by $CO_2$-TPD analysis (Fig. S1 and Table S1), which revealed systematically controlled basic properties. Each catalyst exhibited a distinct $CO_2$ desorption profile depending on the type of metal oxide, with the exception of the 1BaO/Z40. The 1BaO/Z40 showed no discernible $CO_2$ desorption peak, which may be attributed to the high thermal stability of $BaCO_3$. Since $BaCO_3$ decomposes into BaO and $CO_2$ at temperatures above 1300 °C, [51] $CO_2$ desorption from 1BaO/Z40 may occur beyond the upper limit of the TPD measurement range (950 °C). Based on $CO_2$-TPD results, particularly the desorption temperatures, the relative basic strength of the catalysts follows the order: 1BaO/Z40 > 1SrO/Z40 > 1CaO/Z40 > 1MgO/Z40 > Z40.

A series of H-ZSM-5 zeolites with alkaline earth metal oxides, featuring systematically controlled basicity, were tested for the CMTO reaction (Fig. S2). The results indicate that catalytic performance varies significantly depending on the type of impregnated metal oxide. In particular, the $CH_3Cl$ conversion ($X_{CH3Cl}$) showed a strong inverse correlation with base strength. The 1BaO/Z40 catalyst ($T_{max}$ > 950 °C), having the strongest basicity ($CO_2$ desorption temperature: not detected under $CO_2$-TPD condition), exhibited the lowest $CH_3Cl$ conversion of 49.4 %. This was followed by 1SrO/Z40 ($T_{max}$ = 902 °C) at 71.7 %, 1CaO/Z40 (677 °C) at 86.1 %, and 1MgO/Z40 (125 °C) at 99.9 %. Interestingly, the $CH_3Cl$ conversion of 1BaO/Z40 was even lower than that of the unmodified Z40 catalyst (56.8 %), which may be attributed to excessive interaction between the basic BaO sites and the acidic $CH_3Cl$ molecules. Such interaction likely inhibits $CH_3Cl$ at BAS, thereby suppressing catalytic turnover. The correlation between $CO_2$ desorption temperature and $X_{CH3Cl}$ highlights the critical role of base strength in influencing $CH_3Cl$ activation, suggesting that an optimal level of basicity is essential for efficient $CH_3Cl$ conversion. In terms of product selectivity, all catalysts impregnated with alkaline earth metal oxides exhibited similar distributions compared to Z40, implying that the basic sites primarily influence the activation of $CH_3Cl$, but do not significantly alter the subsequent HCP mechanism. Among the tested metal oxides, MgO showed the best overall performance and was therefore selected for further investigation.

A series of H-ZSM-5 zeolites with varying Si/Al ratios and MgO loadings were characterized using XRD, TEM-EDS, $N_2$ physisorption analysis, $NH_3$-TPD, and $CO_2$-TPD (Figs. S7–S14, and Tables S3–S4). Fig. 1 shows representative characterization data of Z40 zeolites with different MgO loadings. XRD confirmed the typical MFI structure (JCPDS card no. 44–0003) that was fully maintained without structural changes upon MgO addition (Figs. 1a and S8b). No distinct MgO peaks were observed in the 2θ region of 42–44°, suggesting effective dispersion of MgO nanoparticles without the formation of bulk MgO. TEM-EDS imaging further verified that the MgO nanoparticles were well-dispersed throughout the Z40 crystal (Figs. 1b and S10).

The structures of H-ZSM-5 zeolites with different Si/Al ratios and MgO loadings were similarly characterized by XRD (Figs. S7–S8) and TEM-EDS (Figs. S9–S11), confirming the preservation of the pristine MFI structure and effective MgO dispersion without formation of bulk MgO crystals regardless of MgO loadings. As MgO loading increased, both the BET surface area and the pore volume decreased gradually (Fig. 1c, and Table S3). The acidic properties varied significantly, as demonstrated by $NH_3$-TPD (Fig. 1d, and Table S4). Higher Si/Al ratios, indicating reduced Al content in the framework, corresponded with a decrease in the number and strength of acidic sites (Fig. S13a, and Table S4). For each H-ZSM-5 zeolite, an increase in MgO loading led to a progressive reduction in both the amount and strength of acid sites (Figs. S13b–S13d, and Table S4). The basic properties were characterized by $CO_2$-TPD (Fig. S14), which revealed distinct $CO_2$ desorption peaks correlated with MgO loading. The pristine zeolites without MgO exhibited no discernible $CO_2$ desorption peaks due to the absence of basic sites, regardless of the Si/Al ratios of each zeolite. In contrast, MgO-loaded zeolites showed a distinct $CO_2$ desorption peak within the temperature range of 115–125 °C, with peak intensity increasing as MgO loading increased to 5 wt%. However, zeolites with 10 wt% MgO exhibited smaller $CO_2$ desorption peaks compared to those with 5 wt% MgO loading, indicating that there is an optimal MgO loading for achieving the desired basic properties in the zeolites. It could also imply that the optimal capacity of zeolites used in this work for supporting MgO with good dispersion would be around 5 wt%.

### 3.2. CMTO reaction using MgO-impregnated zeolite catalysts

Fig. 2 shows the reaction results for H-ZSM-5 zeolites with various Si/Al ratios and MgO loadings in comparison with corresponding H-ZSM-5 zeolites without MgO. The time-dependent $X_{CH3Cl}$ profiles (Figs. 2a–c) and the mean $X_{CH3Cl}$ values during an initial 4-hour reaction period with the mean selectivity values for various products are graphitized for comparison (Figs. 2d–f, and Table 2). The results indicate that catalytic performance varies significantly with the Si/Al ratios of zeolites and the levels of MgO loading. To examine the influence of Si/Al ratios on activity and product selectivity, we first compared the performance of H-ZSM-5 zeolites with varying Si/Al ratios in the absence of MgO. As the Si/Al ratio increased from 15 to 40 and then to 140 (Z15, Z40, and Z140, respectively, in Fig. 2), the mean $X_{CH3Cl}$ value decreased from 90.4 % to 56.8 % and then to 25.5 %, respectively (entries 1, 5, and

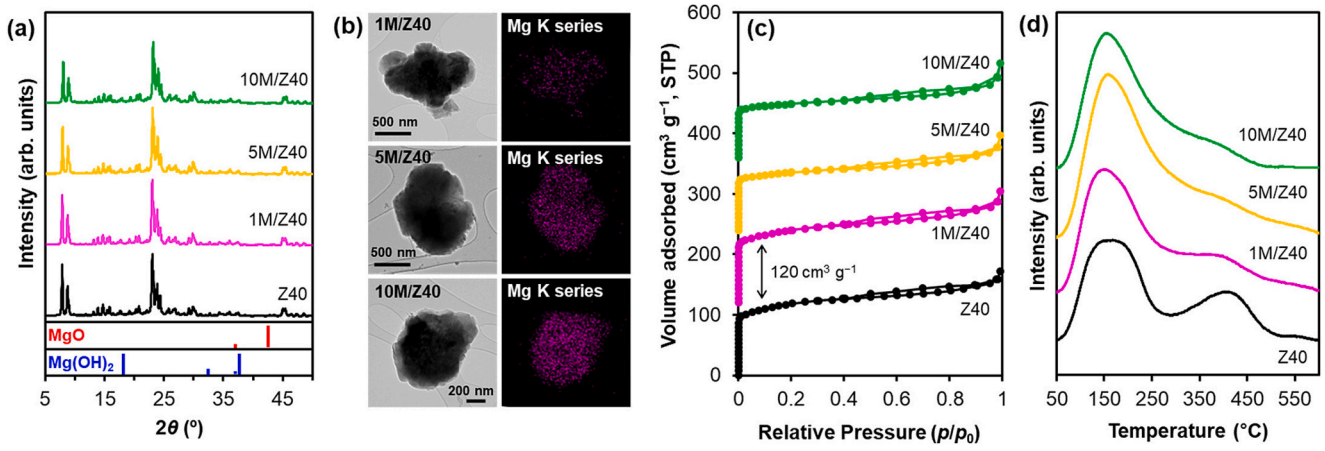


**Fig. 1.** (a) XRD patterns of Z40 zeolites with varying MgO loadings, with vertical (*hkl*) lines indicating peaks corresponding to $Mg(OH)_2$ (blue) and MgO (red) obtained from the JCPDS database. (b) TEM images of Z40 zeolites with varying MgO loadings (left column) and corresponding EDS mapping of the Mg K series (purple, right column) showing the dispersion of MgO throughout the Z40 zeolite crystal. (c) $N_2$ adsorption/desorption isotherms, and (d) $NH_3$ TPD profiles of Z40 zeolites with varying MgO loadings. The corresponding porosity and acidity data are summarized in Tables S2 and S3, respectively.

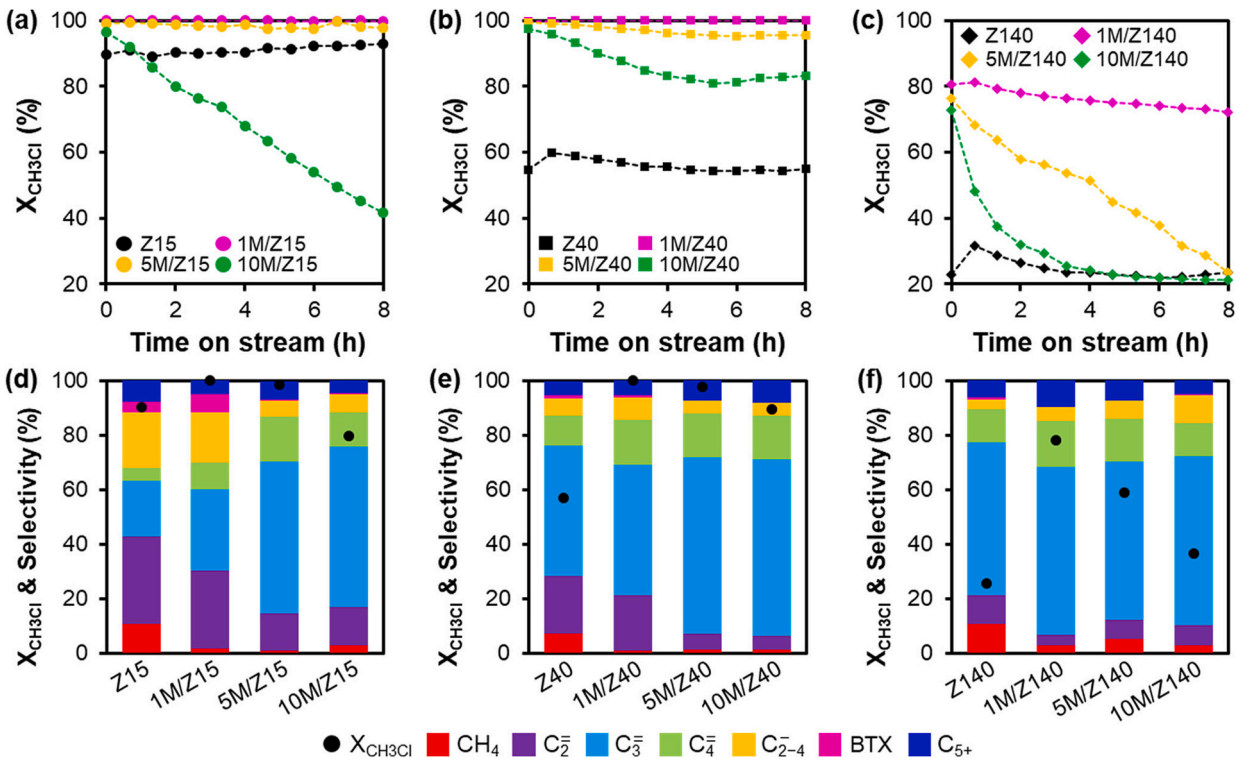


**Fig. 2.** (a–c) Time-dependent $CH_3Cl$ conversion ($X_{CH3Cl}$) profiles of H-ZSM-5 zeolites with various Si/Al ratios and MgO loadings, and (d–f) their corresponding averaged $X_{CH3Cl}$ (black circle) and product selectivity (bar graph with different colors). Mean values were obtained by averaging the reaction results observed during initial reaction period of 4 h, which is also summarized in Table 2.

**Table 2**
Reaction results of H-ZSM-5 zeolites with various Si/Al ratios and MgO loadings in comparison with corresponding H-ZSM-5 zeolites without MgO under flow rates of 2.0 $cm^3\ min^{-1}$ for $CH_3Cl$ and 48.0 $cm^3\ min^{-1}$ for $N_2$. The table presents mean values obtained by averaging the reaction results observed during initial reaction period of 4 h.

| Entry | Catalyst | $X_{CH3Cl}$ (%) | Selectivity (%) | | | | | | | | | | | |
|---|---|---|---|---|---|---|---|---|---|---|---|---|---|---|
| | | | $CH_4$ | $C_2^=$ | $C_3^=$ | $C_4^=$ | $C_{2-4}^=$ | $C_2^-$ | $C_3^-$ | $C_4^-$ | $C_{2-4}^-$ | BTX | $C_{5+}$ | Total |
| 1 | Z15 | 90.4 | 10.9 | 32.0 | 20.4 | 4.7 | 57.1 | 0.9 | 13.1 | 6.4 | 20.4 | 4.0 | 7.6 | 100 |
| 2 | 1M/Z15 | 99.9 | 1.6 | 28.8 | 29.7 | 9.9 | 68.4 | 0.6 | 8.1 | 9.7 | 18.4 | 6.6 | 5.0 | 100 |
| 3 | 5M/Z15 | 98.6 | 0.8 | 13.9 | 55.4 | 16.6 | 85.9 | 0 | 0.7 | 5.2 | 5.9 | 0.6 | 6.8 | 100 |
| 4 | 10M/Z15 | 79.5 | 3.0 | 14.0 | 58.9 | 12.6 | 85.5 | 0.1 | 1.5 | 4.9 | 6.5 | 0.3 | 4.7 | 100 |
| 5 | Z40 | 56.8 | 7.3 | 21.1 | 47.9 | 11.0 | 80.0 | 0.1 | 1.3 | 4.8 | 6.2 | 0.9 | 5.6 | 100 |
| 6 | 1M/Z40 | 99.9 | 1.1 | 20.3 | 47.7 | 16.5 | 84.5 | 0.1 | 1.2 | 6.7 | 8.0 | 1.1 | 5.3 | 100 |
| 7 | 5M/Z40 | 97.8 | 1.4 | 5.8 | 64.5 | 16.2 | 86.5 | 0 | 0.1 | 4.7 | 4.8 | 0.1 | 7.2 | 100 |
| 8 | 10M/Z40 | 89.3 | 1.3 | 5.1 | 64.5 | 16.2 | 85.8 | 0 | 0.1 | 4.6 | 4.7 | 0.1 | 8.1 | 100 |
| 9 | Z140 | 25.5 | 10.6 | 10.9 | 55.9 | 12.2 | 79.0 | 0.1 | 0.2 | 3.1 | 3.4 | 0.9 | 6.1 | 100 |
| 10 | 1M/Z140 | 78.0 | 2.8 | 4.0 | 61.5 | 16.9 | 82.4 | 0 | 0.1 | 4.9 | 5.0 | 0.2 | 9.6 | 100 |
| 11 | 5M/Z140 | 59.1 | 5.2 | 7.0 | 57.9 | 15.9 | 80.8 | 0 | 0.6 | 6.0 | 6.6 | 0 | 7.4 | 100 |
| 12 | 10M/Z140 | 36.6 | 2.9 | 7.6 | 61.6 | 12.2 | 81.4 | 0.1 | 1.1 | 9.2 | 10.4 | 0.1 | 5.2 | 100 |

9, respectively, in Table 2). This suggests that the acidic sites in the zeolite framework play a major role in catalyzing $CH_3Cl$ conversion.

Product selectivity was also strongly influenced by zeolite acidity. The Z15 zeolite, which exhibited the highest $X_{CH3Cl}$, produced significantly more paraffinic and aromatic products, with 20.4 % of $C_{2-4}^-$ and 4.0 % of BTX, respectively. In contrast, Z40 and Z140 zeolites produced less than 10 % of paraffinic $C_{2-4}^-$ and less than 1 % of BTX (entries 1, 5, and 9, respectively, in Table 2). Regarding olefinic products, Z15 produced only 57.1 % of $C_{2-4}^=$, while Z40 and Z140 produced significantly more $C_{2-4}^=$ with 80.0 % and 79.0 %, respectively (entries 1, 5, and 9, respectively, in Table 2). The product distribution, with a dominant formation of $C_{2-4}^=$ on H-ZSM-5 zeolites, aligns with the HCP mechanism previously reported in MTO and CMTO studies using MFI zeolites [52,53].

Erichsen et al., as well as our own research, have shown that the dual cycles (HCP mechanism) are influenced by the acidic properties of the catalyst [13,54,55]. Specifically, weaker acid strength and lower acid density favor the alkene cycle, promoting the formation of $C_3^=$ and $C_4^=$ rather than $C_2^=$ [13,52,55]. In this work, both the strength and the density of acid sites decreased with increasing Si/Al ratios (Fig. S13a, and Table S4). Consistent with these observations, $C_3^=$ and $C_4^=$ selectivity increased, while $C_2^=$ selectivity decreased with the following order of Z15, Z40, and Z140 zeolites (entries 1, 5, and 9, respectively, in Table 2). In terms of total light olefin ($C_{2-4}^=$) selectivity, both Z40 and Z140 catalysts exhibited considerably higher selectivity than Z15 catalyst, indicating that variations in olefin and paraffin selectivity with different Si/Al ratios are primarily influenced by secondary reactions, such as hydrogen transfer and aromatization, occurring on the strong BAS [52].

Compared to bare H-ZSM-5 zeolites without MgO, the addition of MgO led to dramatic changes in $X_{CH3Cl}$ and product selectivity.

Regardless of MgO loadings in H-ZSM-5 zeolites, all MgO-impregnated H-ZSM-5 samples commonly exhibited higher $X_{CH3Cl}$ and $C_{2-4}^{=}$ selectivity, and a decrease in $CH_4$ selectivity, compared to the bare H-ZSM-5 zeolites without MgO (Fig. 2, and Table 2). Specifically, at an MgO loading of 1 wt%, the 1M/Z15, 1M/Z40, and 1M/Z140 catalysts achieved mean $X_{CH3Cl}$ values of 99.9 %, 99.9 %, and 78.0 %, respectively (entries 2, 6, and 10, respectively, in Table 2). Notably, the addition of only 1 wt% MgO nearly doubled and tripled the mean $X_{CH3Cl}$ values for 1M/Z40 and 1M/Z140, respectively. However, further increase in MgO loading did not correspond to proportional enhancements in $X_{CH3Cl}$. Mean $X_{CH3Cl}$ values decreased as MgO loading increased further to 5 and 10 wt%, and this trend was observed in all MgO-impregnated H-ZSM-5 samples. This suggests the existence of an optimal MgO loading for promoting catalytic interplays between MgO and the zeolite.

Catalyst lifetime was dramatically affected by the Si/Al ratios of zeolites and the MgO loadings. In most cases, the addition of MgO to the H-ZSM-5 zeolites increased the deactivation rate (Figs. 2a–c). Specifically, the slopes of the time-dependent $X_{CH3Cl}$ profiles became more negative as MgO loading increased from 1 wt% to 5 wt% and then to 10 wt%, indicating a faster deactivation rate with higher MgO loadings. Although appreciable deactivation was not observed in the 1M/Z15 (pink profile in Fig. 2a, and Fig. S15d) and 1M/Z40 catalysts (pink profile in Fig. 2b, and Fig. S15e), the 1M/Z140 catalyst showed a gradual decrease in $X_{CH3Cl}$ over 8 h of reaction (pink profile in Fig. 2c, and Fig. S15f). Compared to the 1 wt% of MgO loading, 5 wt% loading increased the deactivation rate higher, in which the 5M/Z140 catalyst showed the fastest deactivation among 5M/Z catalysts (yellow profile in Fig. 2c, and Fig. S15i). When the MgO loading was further increased to 10 wt%, all catalysts showed significantly faster deactivation, with the 10M/Z140 catalyst displaying an especially rapid deactivation rate, marked by an exponential decline in $X_{CH3Cl}$ during the initial reaction period (green profile in Fig. 2c, and Fig. S15l). These trends indicate that while optimal MgO loading can positively impact catalytic performance, excessive MgO loading decreases catalyst activity and accelerates deactivation. The corresponding characterizations of spent catalysts, including XRD, TGA, and ICP analyses, are presented in Fig. S16, Fig. S17, and Table S5, respectively. The XRD and TGA results suggest that deactivation is primarily attributed to carbon deposition, which became more pronounced with increasing MgO loading. In contrast, the ICP results confirm that there was no significant Mg loss, indicating that the Mg content was well retained after the reaction.

In terms of product selectivity, with a 1 wt% MgO loading, all 1M/Z catalysts commonly exhibited a notable shift in product distribution, showing increased selectivity for $C_3^{=}$ and $C_4^{=}$ and decreased selectivity for $CH_4$, $C_2^{-}$, $C_3^{-}$, and $C_2^{=}$, compared to bare H-ZSM-5 zeolites without MgO. For example, the 1M/Z15 catalyst showed decreases in selectivity for $CH_4$ (10.9 % → 1.6 %), $C_2^{-}$ (0.9 % → 0.6 %), $C_3^{-}$ (13.1 % → 8.1 %), and $C_2^{=}$ (32.0 % → 28.8 %), along with increases in selectivity for $C_3^{=}$ (20.4 % → 29.7 %) and $C_4^{=}$ (4.7 % → 9.9 %) (entries 1–2 in Table 2). In overall, $C_{2-4}^{=}$ selectivity increased from 57.1 % to 68.4 % (entries 1–2 in Table 2). The selectivity shift towards higher olefins with decreased $C_2^{=}$ selectivity is consistent with the systematic changes in product selectivity observed with varying acid strength and density among Z15, Z40, and Z140 catalysts, as discussed above. Notably, the 1 wt% MgO addition to Z15 decreased both the strength and density of acid sites (Fig. S13b, and Table S4), altering the product selectivity. This suggests that MgO impregnation modified the acidic properties of the catalyst, thus affecting the CMTO reaction mechanism and shifting selectivity ratios among light olefins.

However, compared to 1M/Z15 zeolite, the addition of MgO to the Z140 zeolite resulted in much smaller changes in product distribution, even at a 10 wt% of MgO loading (Fig. 2f, and entries 10–12 in Table 2). This can be attributed to the weaker acid strength and lower acid density of the Z140 framework relative to Z15 (Fig. S13a, and Table S4). In contrast, the Z15 and Z40 zeolites, which possess higher acid densities than Z140, exhibited increases in selectivity for $C_3^{=}$ and $C_4^{=}$ as MgO loading increased from 1 wt% to 5 wt% (Figs. 2d, e, and entries 3 and 7 in Table 2). Interestingly, when the MgO loading was further increased to 10 wt%, the product distribution for the 10M/Z40 catalyst remained almost unchanged (Fig. 2e, and entries 7–8 in Table 2), whereas the 10M/Z15 catalyst exhibited a noticeable change, with approximately fourfold increase in selectivity for undesirable $CH_4$ (Fig. 2d, and entries 3–4 in Table 2). $NH_3$-TPD analysis confirmed that MgO addition led to a notable reduction in zeolite acidity compared to the pristine zeolites without MgO (Fig. S13, and Table S4). These findings suggest that the impact of MgO on product selectivity is more pronounced in zeolites with higher acid densities, while the impact of MgO is relatively less pronounced in zeolite with lower acid density.

Among the 12 catalyst sets with varying Si/Al ratios and MgO loadings (Table 2), the enhancement in $X_{CH3Cl}$ due to MgO addition was most pronounced in the 1M/Z140 zeolite, where $X_{CH3Cl}$ nearly tripled from 25.5 % to 78.0 % (entries 9–10 in Table 2). In contrast, the impact of MgO addition on the Z15 zeolite was minimal, as the stronger, denser acid sites overwhelmed the contribution of MgO (entries 1–4 in Table 2). Interestingly, the addition of 5 wt% MgO to the Z40 zeolite resulted in a high $X_{CH3Cl}$ of 97.8 % and the highest $C_{2-4}^{=}$ selectivity of 86.5 % (entry 7 in Table 2), likely due to the balanced catalytic interplays of MgO and acid sites in the 5M/Z40 zeolite. Consequently, this balance effectively bypassed the typical trade-off, achieving simultaneous improvements in $CH_3Cl$ conversion, catalyst lifetime, and $C_{2-4}^{=}$ selectivity.

### 3.3. Origin of MgO-promoted CMTO reaction

The addition of MgO to the H-ZSM-5 zeolites significantly enhanced their intrinsic catalytic performance, breaking typical trade-offs by simultaneously improving $CH_3Cl$ conversion, catalyst lifetime, and light olefin selectivity. To understand the origin of MgO-promoted CMTO reaction, controlled catalyst sets were constructed and characterized comprehensively. Based on the 5M/Z40 zeolite showing the best-balanced catalytic performance, two additional catalysts (i.e., $5M_{ext}$/Z40, and 5M&Z40) were additionally prepared by supporting 5 wt% of MgO selectively on the external surface of Z40, or by physically mixing 5 wt% of MgO with Z40, respectively (Fig. 3). The distinct XRD reflection at a 2θ of 43° for $5M_{ext}$/Z40 and 5M&Z40 catalysts indicates the presence of bulky MgO crystals (Figs. 3a, b). The adsorbed $N_2$ volume of $5M_{ext}$/Z40 at relative pressures below 0.01 was almost identical to that of the Z40 zeolite, suggesting that the micropores were kept vacant without significant micropore filling by MgO (Fig. 3c, and Table S6). TEM-EDS imaging of $5M_{ext}$/Z40 further confirmed that most MgO particles were primarily dispersed on the external surface of Z40 (Fig. 3d). The resultant $5M_{ext}$/Z40 and 5M&Z40 catalysts enable an investigation into the effect of distance between MgO and BAS on the catalytic performance, in comparison with the 5M/Z40 catalyst.

To investigate the role of zeolite acid sites, $PFA_{int}$/Z40 was also prepared by polymerizing furfuryl alcohol selectively within the micropores of Z40. This approach not only filled the zeolite micropores but also screened BAS on the zeolite surface. As a result of the micropore-filling by PFA, $PFA_{int}$/Z40 exhibited a marked decrease in peak intensity in the XRD reflection at a 2θ range of 8–10°, compared to the original Z40 zeolite (Fig. 3a). Additionally, $PFA_{int}$/Z40 exhibited negligible $N_2$ adsorption at relative pressures below 0.01, further confirming effective micropore filling by PFA (Fig. 3c, and Table S6). By screening the BAS in the zeolite framework, the resultant $PFA_{int}$/Z40 catalyst enables the evaluation of BAS effects on catalytic performance, offering a comparative basis against other Z40-based catalysts.

Fig. 4 shows the time-dependent $X_{CH3Cl}$ profiles and mean product selectivity for the tested catalyst sets (see also Fig. S18, and Table S7 for details). Depending on the $X_{CH3Cl}$, the catalysts can be categorized into two groups: those with $X_{CH3Cl} < 3$ %, and those with $X_{CH3Cl} > 20$ %. The former group, with $X_{CH3Cl} < 3$ %, includes (i) the blank test without

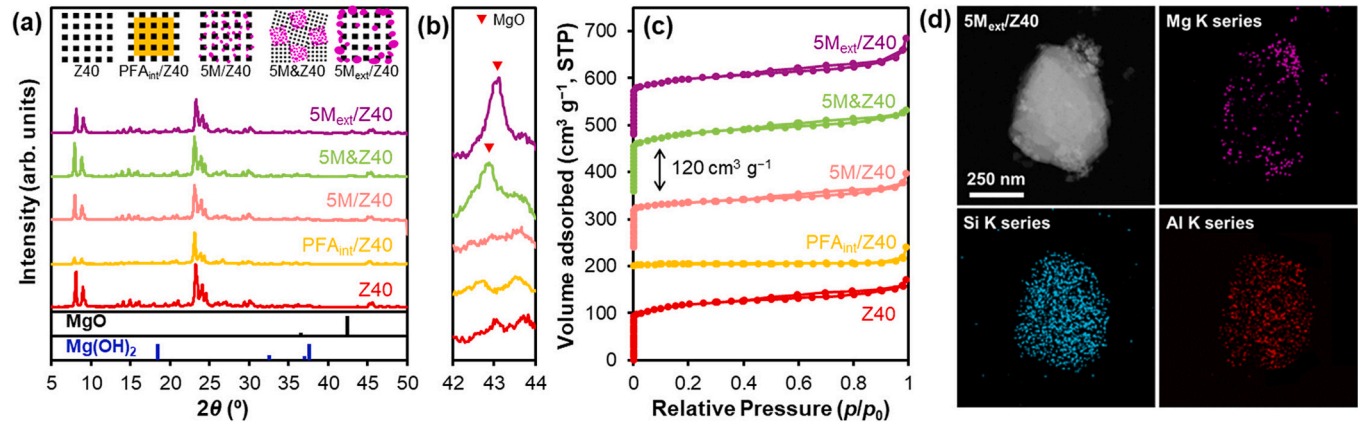


**Fig. 3.** (a) XRD patterns, (b) their magnified view in the 2θ region of 42–44°, and (c) $N_2$ adsorption/desorption isotherms of Z40 (red), PFA$_{int}$/Z40 (yellow), 5M/Z40 (pink), 5M&Z40 (green), and 5M$_{ext}$/Z40 (purple). The vertical (*hkl*) lines in (a) indicate peaks corresponding to $Mg(OH)_2$ (blue) and MgO (black) obtained from the JCPDS database. (d) TEM images of 5M$_{ext}$/Z40 and corresponding EDS mapping of the Mg K (purple), Si K(cyan), and Al K (red) series.

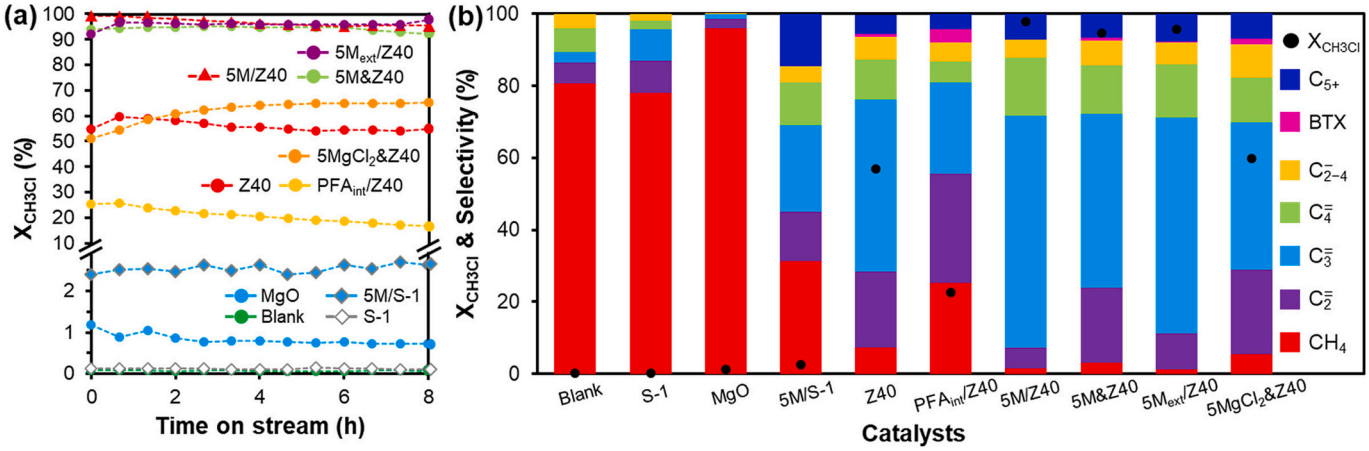


**Fig. 4.** (a) Time-on-stream $CH_3Cl$ conversion ($X_{CH3Cl}$) profiles with (b) mean product selectivity for the tested catalysts. Mean product selectivity observed during initial reaction period of 4 h and summarized in Table S7.

catalyst, (ii) S-1 without MgO, (iii) MgO alone without zeolite, and (iv) 5M/S-1 (entries 1–4 in Table S7). Here, S-1 refers to purely siliceous silicalite-1, a zeolite with the same MFI structure as Z40 but without aluminum, and thus without acid sites. This allows S-1 to be a comparative material for distinguishing the catalytic effects of MgO and BAS of the Z40 zeolite. The latter group, with $X_{CH3Cl} > 20$ %, comprises six different Z40-based catalysts (Fig. 4b, and entries 5–10 in Table S7). The primary difference between the former and the latter groups appears to be the respective absence or presence of BAS.

The BAS-absent group generally exhibited low activity ($X_{CH3Cl} < 3$ %) with $CH_4$ as the major product (Fig. 4b, and entries 1–4 in Table S7), whereas the BAS-present group achieved higher activity with $X_{CH3Cl}$ values ranging from 22.6 % to 97.8 % depending on the Z40-based catalyst structure (Fig. 4b, and entries 5–10 in Table S7). The Z40 catalyst alone showed a mean $X_{CH3Cl}$ of 56.8 %, but this decreased by more than half to 22.6 % in PFA$_{int}$/Z40 catalyst (Fig. 4b, and entries 5–6 in Table S7). In addition, PFA$_{int}$/Z40 catalyst exhibited a lower $C_{2-4}^{=}$ selectivity of 61.5 %, and a higher $CH_4$ selectivity of 25.2 % compared to other Z40-based catalysts. This decrease in $X_{CH3Cl}$ alongside higher $CH_4$ selectivity suggests that PFA filled in the Z40 micropores screened BAS considerably, thus reducing the catalytic contribution of BAS. These findings indicate that the significant performance difference between the two catalyst groups can be attributed to the presence of BAS, which facilitates $CH_3Cl$ dissociation during CMTO reaction.

Interestingly, compared to the Z40 alone, which achieved a mean $X_{CH3Cl}$ of 56.8 % (Fig. 4b, and entry 5 in Table S7), MgO-supported Z40 catalysts prepared using various incorporation methods showed significantly higher mean $X_{CH3Cl}$ values above 90 %, regardless of the method for MgO incorporation (Fig. 4b, and entries 7–9 in Table S7). Only slight differences in $X_{CH3Cl}$ and $C_{2-4}^{=}$ selectivity among MgO-incorporated Z40 catalysts were observed (Fig. 4b, and entries 7–9 in Table S7), indicating that the specific method for MgO incorporation is not critical factor for making enhancements in catalytic performances. However, the presence of MgO clearly contributed to remarkable improvements in both $X_{CH3Cl}$ and $C_{2-4}^{=}$ selectivity within the Z40 catalyst system. The similar $CH_3Cl$ conversion and product selectivity observed among 5M/Z40, 5M&Z40, and 5M$_{ext}$/Z40 catalysts suggest that the CMTO reaction proceeds via a comparable HCP mechanism, regardless of the dispersion position of MgO. Despite the modification of the spatial proximity between MgO and the Brønsted acid sites, no significant differences in catalytic performance, implying that MgO does not directly participate in or alter the acid catalyzed-HCP mechanism itself. In other words, MgO does not function as an independent base catalyst for the HCP pathway. Instead, its role is primarily to interact with $CH_3Cl$, facilitating the formation of activated $CH_3Cl$ species, which are subsequently transferred to Brønsted acid sites where the HCP mechanism proceeds. This interaction enhances $CH_3Cl$ conversion and promotes higher light olefin selectivity, particularly under conditions where the balance between acid and base sites is optimized.

To further validate the proposed role of MgO in $CH_3Cl$ activation and

its non-involvement in the HCP mechanism itself, a comparative MTO reaction was conducted using Z40 and 5M/Z40 catalysts (Fig. S20). Based on the CMTO reaction results, MTO reactions were carried out at two different temperatures: a relatively low temperature (300 °C) to evaluate changes in $CH_3OH$ conversion under conditions where $CH_3OH$ activation is moderately facilitated, and a higher temperature (350 °C) to evaluate the potential contribution of MgO to the HCP mechanism under complete $CH_3OH$ conversion. At 300°C (Figs. S20a and b), a significant difference in $CH_3OH$ conversion was observed. The pristine Z40 catalyst showed moderate $CH_3OH$ conversion that decreased during 480 min of reaction, whereas the 5M/Z40 catalyst exhibited a dramatically low conversion (below 5 %). At 350°C (Figs. S20c and d), while the pristine Z40 catalyst maintained complete $CH_3OH$ conversion without deactivation, the 5M/Z40 catalyst showed decreased conversion of 60 %. Regarding product selectivity, although the results at 300 °C showed differences depending on the presence of MgO, the extremely low $CH_3OH$ conversion with 5M/Z40 catalyst makes the product selectivity data unreliable and unsuitable for meaningful discussion. In contrast, the results at 350 °C, where sufficient $CH_3OH$ conversion was achieved for both catalysts, provide a more valid basis for comparison. Under these conditions, product selectivity was not significantly different in Z40 and 5M/Z40 regardless of MgO, suggesting that the presence of MgO did not alter the reaction pathway or the HCP mechanism. Collectively, these MTO reaction results support the suggestion that MgO does not alter or initiate the HCP mechanism itself but rather facilitates $CH_3Cl$ activation thereby promoting subsequent olefin formation on BAS of the zeolite framework.

To clarify the promoting role of MgO, we further characterized spent catalysts after CMTO reaction. First, the crystallinity of the $5M_{ext}$/Z40 zeolite after the CMTO reaction was analyzed in comparison with 5M/Z40 zeolite (Figs. 5a–c). The MFI structures of both 5M/Z40 and $5M_{ext}$/Z40 zeolites were preserved without significant alterations after the CMTO reaction (Fig. 5a). In addition, any appreciable peak corresponding to $MgCl_2$ was not observed after the CMTO reaction (Fig. 5b). However, a distinct XRD peak in the 2θ range of 42 – 44°, corresponding to MgO [200], which was visible in the pristine $5M_{ext}$/Z40 catalyst, nearly disappeared completely after the reaction (Fig. 5c). Given that 5 wt% of MgO should still be present on Z40, the disappearance of XRD reflection may infer that MgO may have re-dispersed throughout the Z40 crystal, likely forming MgO nanocrystals or their derivative nanostructures.

Second, XPS analysis further supported the observations in XRD, in which an Mg 2p peak in the pristine $5M_{ext}$/Z40 catalyst was observed at binding energy of 50.5 eV with the highest intensity (Fig. 5d). Compared to the Mg 2p peaks of other catalysts, the highest intense Mg 2p peak of the pristine $5M_{ext}$/Z40 catalyst suggests that the majority of MgO was highly concentrated and exposed on the external surface of Z40 catalyst. However, after the CMTO reaction, this peak was shifted to a higher binding energy of 51.2 eV with significant decrease in intensity. This shift indicates that the large MgO crystals on the external surface of Z40 zeolite were re-dispersed throughout the Z40 framework, thereby significantly reducing the concentration of MgO on the external surface. A similar increase in binding energy for the Mg 2p XPS peak with significant decrease in intensity was also observed in 5M/Z40 (50.0 → 51.4 eV) catalyst after the CMTO reaction (Fig. 5d), indicating changes in chemical bonding around Mg atoms. It should be noted that all the components of Si, Al, and Mg were preserved in the 5M/Z40 catalyst after CMTO reaction, indicating that the disappearance of the MgO peaks in the XRD and XPS spectra was not due to the loss of Mg in the catalyst (Table S5).

The changes in chemical environment of Mg atoms could be clarified more by the appearance of a new XPS peak in the Cl 2p XPS region, observed in both 5M/Z40 and $5M_{ext}$/Z40 catalysts after the CMTO reaction (Fig. 5e). The presence of the Cl 2p XPS peak suggests that $CH_3Cl$, its dissociated species, and/or chlorinated products accumulated on the catalyst surface during the CMTO reaction. The electronegative Cl species likely bind to MgO, probably through the formation of $MgCl_2$ and/or $(MgO)Cl_x$ species, which decreased electron density around Mg atoms and thereby shifted the Mg 2p binding energy higher. If $MgCl_2$ species was dominantly formed, the catalytic cycle of MgO-impregnated Z40 zeolites might be terminated, since the chemical bond of Mg – Cl is too strong to be dissociated. In contrast, if $(MgO)Cl_x$ species was dominantly formed, it would be expected that the catalytic cycle would be maintained since the chemical bond of (MgO) – Cl is weak so that the adsorption/desorption of Cl species could be reversible. Based on this, the promoted catalytic activity with sustainable performance of Z40 zeolites with 5 wt% of MgO loadings (Fig. 4a) could imply that the $MgCl_2$ species was rarely formed during the CMTO reaction. Furthermore, we extended the reaction time further to 80 h using 5M/Z40 catalyst, which confirmed sustainable catalytic performance without deactivation and structural changes of catalyst (Fig. S19). XRD patterns of the pristine and spent 5M/Z40 catalysts show no significant

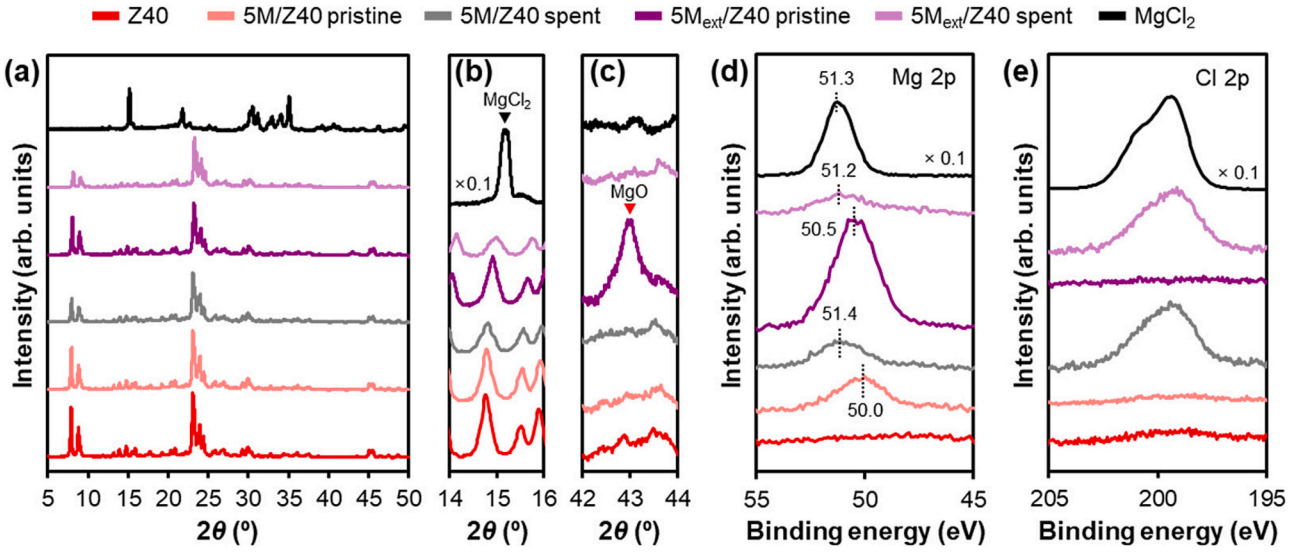


**Fig. 5.** (a) XRD patterns, their magnified view in the 2θ region of (b) 14 – 16° and (c) 42 – 44°, and XPS spectra in the binding energy regions of (d) Mg 2p and (e) Cl 2p of 5 M/Z40 and $5M_{ext}$/Z40 before and after the CMTO reaction (denoted as pristine and spent, respectively), in comparison with pristine Z40 without MgO and commercial $MgCl_2$.

difference, indicating that the overall crystalline structure was preserved during the reaction. In the FT-IR analysis, the pristine 5M/Z40 catalyst exhibits a characteristic Mg–O stretching vibration band at 606 $cm^{-1}$. After the reaction, the intensity of this band decreased noticeably, suggesting a partial transformation of MgO. The fact that the Mg–O vibration did not completely disappear implies that MgO was not fully converted into $MgCl_2$ during the reaction but may instead have formed $(MgO)Cl_x$ species, providing indirect evidence for their presence. In particular, when we tested $5MgCl_2$&Z40 in the CMTO reaction, its catalytic activity ($X_{CH3Cl}$) and the product distribution were similar with those of pure Z40 zeolite without MgO (Fig. 4, and entry 10 in Table S7), indicating that the synergistic role of $MgCl_2$ is almost negligible while the BAS on Z40 zeolite is governing the catalysis. The associated interpretation of XRD, XPS, FT-IR, and reaction data could conclude that the MgO was not converted to $MgCl_2$ species but dominantly converted to $(MgO)Cl_x$ species, which could contribute the sustainable catalytic performance with enhanced activity.

### 3.4. Mechanistic view of MgO-promoted CMTO reaction

The formation of C–C bonds in the CMTO reaction is generally understood to proceed via the HCP mechanism, involving methylation, oligomerization, and cyclization steps over BAS, as widely accepted in previous studies [13–16,50,53]. In this study, we do not aim to propose a new reaction pathway beyond the HCP, but rather to control the established mechanism through the introduction of acid-base bifunctionality.

To better understand the CMTO reaction process, we monitored changes occurring on the catalyst surface in real-time using the DRIFTS technique. Fig. 6 shows the DRIFTS spectra for the 5M/Z40 (Figs. 6a–c), $5M_{ext}$/Z40 (Figs. 6d–f), Z40 (Figs. 6g–i), and MgO (Figs. 6j–l) catalysts in three wavenumber regions under CMTO reaction conditions. This approach enables real-time tracking of the dynamic interactions of reactant and intermediate species to the catalyst surface during the reaction. Among the tested catalysts, the most dramatic color changes in the DRIFTS contour map were observed for 5M/Z40 catalyst (Figs. 6a–c), indicating significant alternations in the chemical environment on its surface compared to the other catalysts. Specifically, in the 3400–3800 $cm^{-1}$ range, negative absorption peaks were observed (blue color in Fig. 6a), which is attributed to the strong adsorption of $CH_3Cl$ on the hydroxyl (–OH) group of BAS [56–58]. The electronegative Cl in $CH_3Cl$ may bind to the BAS, substantially affecting the intrinsic

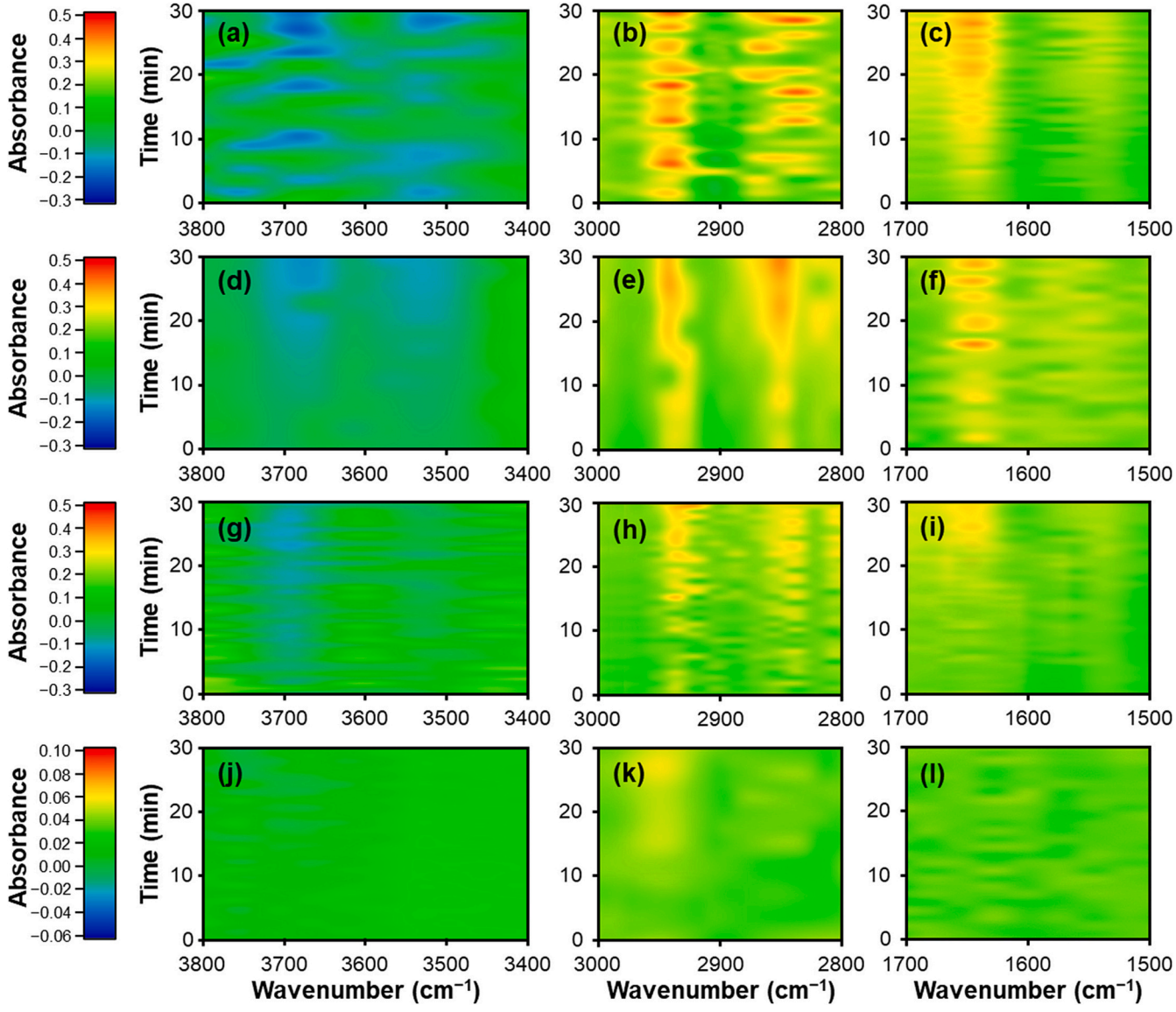


**Fig. 6.** DRIFTS contour map spectra of (a–c) 5M/Z40, (d–f) $5M_{ext}$/Z40, (g–i) Z40, and (j–l) MgO measured in three different wavenumber regions under CMTO reaction condition.

vibration of the hydroxyl. In the 2800–3000 $cm^{-1}$ range, positive absorption peaks with yellow to red colors appeared, likely due to the vibrations of C–H bonds in methyl or terminal aliphatic groups, [56–58] suggesting dynamic $CH_3Cl$ activation on the surface of the 5M/Z40 catalyst (Fig. 6b). In the 1500–1600 $cm^{-1}$ and 1600–1700 $cm^{-1}$ ranges, which correspond to C=C bonds in alkylated aromatics or olefins, respectively, [57,58] strong positive absorption peaks with yellow and red colors were observed predominantly in the olefin-based region (1600–1700 $cm^{-1}$), whereas less intense peaks appeared in the aromatic-based region (1500–1600 $cm^{-1}$) (Fig. 6c). This suggests that olefins were more concentrated on the surface of the 5M/Z40 catalyst than aromatic compounds, consistent with the high olefin selectivity achieved by 5M/Z40 (Fig. 4, and entry 7 in Table S7).

Compared to the 5M/Z40 catalyst, the absorption peak intensities for $5M_{ext}$/Z40, Z40 and MgO were notably weaker. First, in the 3400–3800 $cm^{-1}$ range, weak absorption peaks were observed only for the $5M_{ext}$/Z40 (Fig. 6d) and Z40 (Fig. 6g) catalysts, whereas no absorption peak was observed for MgO (Fig. 6j). The BAS on Z40 may facilitate $Cl^-$ dissociation from $CH_3Cl$, altering the intrinsic vibration of the hydroxyl group on BAS. This observation strongly supports the role of BAS on Z40 as a primary catalyst for $CH_3Cl$ activation, with the strongest $CH_3Cl$ activation observed in the 5M/Z40 catalyst (Fig. 6d). Second, in the 2800–3000 $cm^{-1}$ range, all tested catalysts exhibited positive absorption peaks with yellow color. Although the peak for MgO was the weakest with bright yellow color (Fig. 6k), this absorption peak suggests the presence of C–H vibrations from methyl or terminal aliphatic groups generated during the $CH_3Cl$ activation on MgO. Specifically, the MgO surface, acting as a Lewis base due to its oxygen anions, can interact with Lewis acids. Therefore, similar to the catalytic role of BAS on Z40 zeolite, $CH_3Cl$ seemed to be dissociated heterolytically on MgO into $CH_3^+$ and $Cl^-$, acting as Lewis acid and base, respectively, to form methoxy ($–OCH_3$) and $(MgO)Cl_x$ species on the MgO surface. Note that the formation of $(MgO)Cl_x$ was also suggested by catalytic reactions and XPS analysis (Figs. 4 and 5d, e). The evidence of $CH_3Cl$ activation on MgO observed in the DRIFTS spectra may explain why MgO alone can facilitate CMTO reaction, although its activity is much lower than that of the zeolite-based catalysts (Fig. 4, and entry 3 in Table S7).

The comprehensive characterization above clarified that both MgO and BAS of Z40 zeolite contributed synergistically to $CH_3Cl$ activation, resulting in enhanced catalytic performance. The catalytic interplays between these active sites are crucial for promoting the CMTO reaction. Through additional controlled FT–IR studies below (Fig. 7), we further explored how MgO enhances catalytic performance while the BAS on Z40 zeolite serves as the primary catalytic site. It has been reported that supported transition metal catalysts can induce a spillover of methyl species, analogous to the hydrogen spillover phenomenon observed on the noble metal nanoparticle supported on transition metal oxides [59,60]. Similarly, we hypothesized that MgO enabled spillover of activated methyl species originating from the $CH_3Cl$ activation on the MgO surface. To test this hypothesis, we investigated $CH_3Cl$ activation on silicalite-1 (i.e., S-1) with and without MgO using FT-IR spectroscopy. When $CH_3Cl$ was introduced to S-1 alone, no appreciable peaks appeared in the 2600–3200 $cm^{-1}$ region (compare yellow and grey spectra in Fig. 7), indicating that S-1 alone did not activate $CH_3Cl$, consistent with the reaction test shown above (Fig. 4, and entry 2 in Table S7). However, when $CH_3Cl$ was introduced to MgO supported S-1 (i.e., 5M/S-1), new FT-IR peaks appeared (compare green and black spectra in Fig. 7). Previous studies have shown that S-1 can activate $CH_3OH$ by forming $Si–O–CH_3$ on its surface, as evidenced by FT-IR (blue spectra in Fig. 7). By comparing the FT-IR spectra of $CH_3OH$-activated S-1 with those of $CH_3Cl$-activated 5M/S-1, we identified the new peaks as C–H stretching modes in $Si–O–CH_3$, suggesting that the $CH_3Cl$ activation on 5M/S-1 also involves the formation of $Si–O–CH_3$ by spillover of methyl species from MgO to $SiO_2$ (compare green and blue spectra in Fig. 7).

Summarizing the controlled FT-IR studies alongside the evidence in DRIFTS, we could conclude that $CH_3Cl$ is initially activated on the MgO surface, with the resultant activated methyl species subsequently spilling over to the S-1 surface, as indicated by the formation of $Si–O–CH_3$, while Cl species remains as a $(MgO)Cl_x$ species. Similarly, MgO activates $CH_3Cl$ via Lewis acid-base interaction and enables the spillover of activated methyl species to the BAS on the Z40 zeolite, while Z40 also independently activates $CH_3Cl$ (Scheme 1). This synergistic activation may significantly enhance the overall catalytic performance.

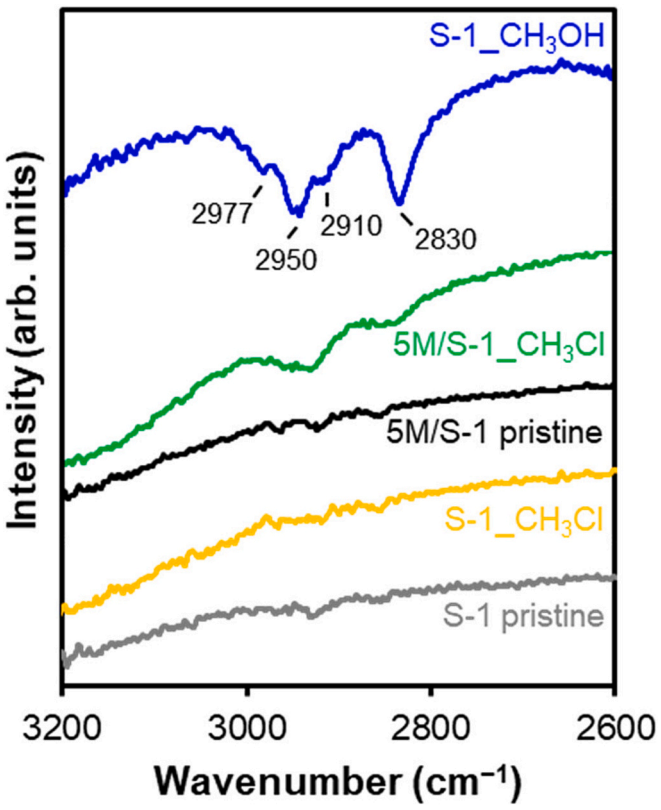


**Fig. 7.** FT-IR spectra of S-1 pristine (grey), $CH_3Cl$-treated S-1_$CH_3Cl$ (yellow), 5M/S-1 pristine (black), $CH_3Cl$-treated 5M/S-1_$CH_3Cl$ (green), and $CH_3OH$-treated S-1_$CH_3OH$ (blue) from bottom to top.

## 4. Conclusions

This study elucidated the synergistic catalytic acid–base interplay between Brønsted acid sites (BAS) in ZSM-5 zeolites and Lewis basic sites in MgO for the efficient conversion of chloromethane ($CH_3Cl$) to light olefins. Through systematic catalyst design and comprehensive characterization, we demonstrated that MgO plays a crucial role in $CH_3Cl$ activation, facilitating methyl species spillover to BAS, which enhances overall catalytic performance. The optimal incorporation of MgO effectively balanced catalytic activity, catalyst lifetime, and olefin selectivity, overcoming the conventional trade-offs in CMTO reactions. Notably, only 1 wt% MgO addition significantly boosted $CH_3Cl$ conversion from 56.8 % to 99.9 %, while 5 wt% MgO yielded an unprecedented 86.5 % selectivity for $C_{2-4}^{=}$ olefins, confirming the synergistic role of MgO in promoting catalytic activity of zeolite. DRIFTS and FT–IR analyses provided direct evidence of $CH_3Cl$ activation on MgO, with subsequent methyl spillover onto BAS, a process reminiscent of hydrogen spillover in metal-catalyzed reactions. The findings reveal that MgO incorporation does not merely alter acidity but introduces a cooperative reaction mechanism that sustains catalytic activity while minimizing deactivation. These insights pave the way for a new approach in $C_1$ chemistry, where controlled spillover phenomena can enhance catalyst performance for selective hydrocarbon

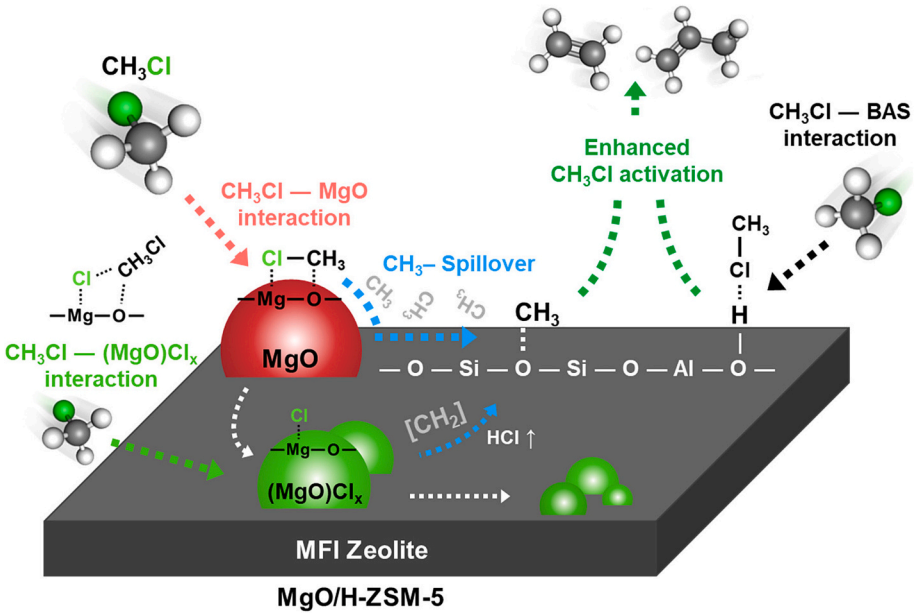


**Scheme 1.** Schematic representation of the synergistic activation of $CH_3Cl$ on the MgO/H-ZSM-5 catalyst. The $CH_3Cl$–BAS interaction represents the activation of $CH_3Cl$ on the Brønsted acid sites of ZSM-5 zeolite, forming –OH–$ClCH_3$ bond. The $CH_3Cl$–MgO interaction represents the activation of $CH_3Cl$ on the surface of magnesium oxide, forming Mg–Cl bond and O–$CH_3$ bond and then, $CH_3$– spills over to zeolite surface to form methoxy species. During the process of the $CH_3Cl$–MgO interaction, MgO is redispersed on the zeolite surface, forming $(MgO)Cl_x$ species. The $CH_3Cl$–$(MgO)Cl_x$ interaction represents the activation of $CH_3Cl$ on $(MgO)Cl_x$ species. Electronegative Cl and O species bind to $CH_3Cl$, resulting in the formation of hydrocarbon pool species ($CH_2$) and HCl.

transformations. Future studies may extend this concept to other $C_1$ molecules, further broadening the scope of spillover-mediated catalytic processes in sustainable olefin production.

## Author contribution

The manuscript was written through contributions of all authors. All authors have given approval to the final version of the manuscript.

## CRediT authorship contribution statement

**Seungdon Kwon:** Writing – review & editing, Writing – original draft, Investigation, Data curation. **Jun Hyeok Heo:** Investigation, Data curation. **Changgi Kim:** Investigation, Data curation. **Woosung Leem:** Investigation, Data curation. **Hanbit Jang:** Investigation, Data curation. **Kyungsu Na:** Writing – review & editing, Writing – original draft, Supervision, Project administration, Investigation, Funding acquisition, Data curation, Conceptualization.

## Funding

This work was supported by the National Research Foundation of Korea (NRF) grant funded by the Korea government (MSIT) (RS-2024–00466475 and RS-2024–00349276).

## Declaration of competing interest

The authors declare that they have no known competing financial interests or personal relationships that could have appeared to influence the work reported in this paper.

## Acknowledgments

The authors are grateful to the Center of Research Facilities at the Chonnam National University for their assistance in the TEM–EDS and XPS analyses.

## Appendix A. Supplementary material

Supplementary data to this article can be found online at https://doi.org/10.1016/j.jcat.2025.116464.

## Data availability

Supplementary Material was submitted for data share.

All data are available in the main text or the supplementary materials.

## References

[1] I. Amghizar, L.A. Vandewalle, K.M. Van Geem, G.B. Marin, New trends in olefin production, Engineering 3 (2017) 171–178, https://doi.org/10.1016/J.ENG.2017.02.006.
[2] B. Wu, Y. Shi, Z. Zhang, Z. Wang, S. Sun, L. Wang, H. Huang, L. Zhang, Y. Wu, Stabilizing ultra-small bimetallic PtSn clusters within S-1 crystals for effective propane dehydrogenation with low Pt loading, Chem. Eng. J. 498 (2024) 155205, https://doi.org/10.1016/j.cej.2024.155205.
[3] M.A. Sanhoob, O. Muraza, E.N. Shafei, T. Yokoi, K. Choi, Steam catalytic cracking of heavy naphtha (C12) to high octane naphtha over B-MFI zeolite, Appl. Catal. B 210 (2017) 432–443, https://doi.org/10.1016/j.apcatb.2017.04.001.
[4] S. Chen, X. Chang, G. Sun, T. Zhang, Y. Xu, Y. Wang, C. Pei, J. Gong, Propane dehydrogenation: catalyst development, new chemistry, and emerging technologies, Chem. Soc. Rev. 50 (2021) 3315–3354, https://doi.org/10.1039/D0CS00814A.
[5] E.T.C. Vogt, B.M. Weckhuysen, Fluid catalytic cracking: recent developments on the grand old lady of zeolite catalysis, Chem. Soc. Rev. 44 (2015) 7342–7370, https://doi.org/10.1039/C5CS00376H.
[6] Y. Wei, D. Zhang, Z. Liu, B.L. Su, Methyl halide to olefins and gasoline over zeolites and SAPO catalysts: a new route of MTO and MTG, Chin. J. Catal. 33 (2012) 11–21, https://doi.org/10.1016/S1872-2067(10)60303-8.
[7] I. Yarulina, A.D. Chowdhury, F. Meirer, B.M. Weckhuysen, J. Gascon, Recent trends and fundamental insights in the methanol-to-hydrocarbons process, Nat. Catal. 1 (2018) 398–411, https://doi.org/10.1038/s41929-018-0078-5.
[8] T. Papalas, A.N. Antzaras, A.A. Lemonidou, Unravelling the role of Co in mixed Ni-Co oxygen carriers/catalysts for $H_2$ production via sorption enhanced steam methane reforming coupled with chemical looping, Appl. Catal. B 347 (2024) 123777, https://doi.org/10.1016/j.apcatb.2024.123777.
[9] Y. Xue, J. Li, P. Wang, X. Cui, H. Zheng, Y. Niu, M. Dong, Z. Qin, J. Wang, W. Fan, Regulating Al distribution of ZSM-5 by Sn incorporation for improving catalytic properties in methanol to olefins, Appl. Catal. B 280 (2021) 119391, https://doi.org/10.1016/j.apcatb.2020.119391.

[10] S.M. Sadrameli, Thermal/catalytic cracking of liquid hydrocarbons for the production of olefins: a state-of-the-art review II: catalytic cracking review, Fuel 173 (2016) 285–297, https://doi.org/10.1016/j.fuel.2016.01.047.
[11] B. Terlingen, R. Oord, M. Ahr, E. Hutter, C.V. Lare, B.M. Weckhuysen, Mechanistic insights into the lanthanide-catalyzed oxychlorination of methane as revealed by operando spectroscopy, ACS Catal. 11 (2021) 10574–10588, https://doi.org/10.1021/acscatal.1c00393.
[12] S. Svelle, S. Aravinthan, M. Bjørgen, K.P. Lillerud, S. Kolboe, I.M. Dahl, U. Olsbye, The methyl halide to hydrocarbon reaction over H-SAPO-34, J. Catal. 241 (2006) 243–254, https://doi.org/10.1016/j.cat.2006.04.013.
[13] S. Kwon, Y. Kim, T.W. Kim, H.J. Chae, K. Na, Chloromethane-to-olefin using metal oxide-impregnated small-pore SSZ-13 zeolites with controlled acidity, reactant affinity, and reaction pathway, Chem. Eng. J. 474 (2023) 145851, https://doi.org/10.1016/j.cej.2023.145851.
[14] Y. Wei, D. Zhang, Z. Liu, B.L. Su, Highly efficient catalytic conversion of chloromethane to light olefins over HSAPO-34 as studied by catalytic testing and in situ FTIR, Catalysis 238 (2006) 46–57, https://doi.org/10.1016/j.jcat.2005.11.021.
[15] T. Wang, C. Yang, S. Li, G. Yu, Z. Liu, H. Wang, P. Gao, Y. Sun, Solvent-free synthesis of Mg-incorporated nanocrystalline SAPO-34 zeolites via natural clay for chloromethane-to-olefin conversion, ACS Sustain. Chem. Eng. 8 (2020) 4185–4193, https://doi.org/10.1021/acssuschemeng.9b07129.
[16] J. Kim, Y. Ryou, G. Hwang, J. Bang, J. Jung, Y. Bang, D.H. Kim, Oxychlorination of methane over $FeO_x/CeO_2$ catalysts, Korean J. Chem. Eng. 35 (2018) 2185–2190, https://doi.org/10.1007/S11814-018-0135-4.
[17] B. Terlingen, R. Oord, M. Ahr, E.M. Hutter, C. Van Lare, B.M. Weckhuysen, Favoring the ethane oxychlorination reaction over EuOCl by synergistic effects with lanthanum, ACS Catal. 12 (2022) 5698–5710, https://doi.org/10.1021/acscatal.2c00777.
[18] Y. Kim, J. Kim, H.W. Kim, T.W. Kim, H.J. Kim, H. Chang, M.B. Park, H.J. Chae, Sulfated tin oxide as highly selective catalyst for the chlorination of methane to methyl chloride, ACS Catal. 9 (2019) 9398–9410, https://doi.org/10.1021/acscatal.9b02645.
[19] S. Kwon, H.J. Chae, K. Na, Control of methane chlorination with molecular chlorine gas using zeolite catalysts: effects of Si/Al ratio and framework type, Catal. Today 352 (2020) 111–117, https://doi.org/10.1016/j.cattod.2020.01.014.
[20] Y. Kim, M.S. Goh, J. Kim, T.W. Kim, K.E. Jeong, K.S. Ha, K. Na, K.C. Ko, H.J. Chae, Defective graphitic carbon as a high chlorine conversion catalyst for methyl chloride production from methane, J. Ind. Eng. Chem. 122 (2023) 58–67, https://doi.org/10.1016/j.jiec.2023.02.009.
[21] H. Joo, D. Kim, K.S. Lim, Y.N. Choi, K. Na, Selective methane chlorination to methyl chloride by zeolite Y-based catalysts, Solid State Sci. 77 (2018) 74–80, https://doi.org/10.1016/j.solidstatesciences.2018.01.010.
[22] S. Kwon, S. Park, Y. Choi, K.C. Ko, H.J. Chae, K. Na, $CH_4$ chlorination with $Cl_2$ using zeolites having different surface polarities: catalysis descriptors explaining the electrophilic pathway, J. $CO_2$ Util. 42 (2020) 101318, https://doi.org/10.1016/j.jcou.2020.101318.
[23] Y. Choi, S. Park, S. Kwon, K.C. Ko, K. Na, Controlled electropositive catalytic sites on zeolites for achieving high $CH_3Cl$ selectivity via electrophilic $CH_4$ chlorination using $Cl_2$, J. Mater. Chem. A 198 (2022) 24437–24954, https://doi.org/10.1039/D2TA06787K.
[24] Z. Zhang, M. Vanni, X. Wu, P. Hemberger, A. Bodi, S. Mitchell, J. Pérez-Ramirez, CO cofeeding affects product distribution in $CH_3Cl$ coupling over ZSM-5 zeolite: pressure twists the plot, Angew. Chem. Int. Ed. 63 (2024) e202401060, https://doi.org/10.1002/anie.202401060.
[25] T.H. Kim, M.Y. Gim, G. Hwang, J. Bang, D.H. Kim, Effects of Co/Al molar ratio in CoAPSO-34 catalysts on the physicochemical property and catalytic performance in the chloromethane to light olefins reaction, Appl. Catal. A 603 (2020) 117762, https://doi.org/10.1016/j.apcata.2020.117762.
[26] Y.H. Shin, S. Kweon, M.B. Park, H.J. Chae, Comparative study of CHA-and AEI-type zeolytic catalysts for the conversion of chloromethane into light olefins, Korean J. Chem. Eng. 35 (2018) 1433–1440, https://doi.org/10.1007/s11814-018-0050-8.
[27] L. Kong, Z. Jiang, J. Zhao, J. Liu, B. Shen, The synthesis of hierarchical SAPO-34 and its enhanced catalytic performance in chloromethane conversion to light olefins, Catal. Lett. 144 (2014) 1609–1616, https://doi.org/10.1007/s10562-014-1296-3.
[28] M.H. Nilsen, S. Svelle, S. Aravinthan, U. Olsbye, The conversion of chloromethane to light olefins over SAPO-34: the influence of dichloromethane addition, Appl. Catal. A 367 (2009) 23–31, https://doi.org/10.1016/j.apcata.2009.07.047.
[29] M. Gamero, A.T. Aguayo, A. Ateka, P. Pérez-Uriarte, A.G. Gayubo, J. Bilbao, Role of shape selectivity and catalyst acidity in the transformation of chloromethane into light olefins, Ind. Eng. Chem. Res. 54 (2015) 7822–7832, https://doi.org/10.1021/acs.iecr.5b01745.
[30] M. Ibáñez, M. Gamero, J. Ruiz-Martínez, B.M. Weckhuysen, A.T. Aguayo, J. Bilbao, P. Castaño, Simultaneous coking and dealumination of zeolite H-ZSM-5 during the transformation of chloromethane into olefins, Catal. Sci. Technol. 6 (2016) 296–306, https://doi.org/10.1039/C5CY00784D.
[31] P. Lersch, F. Bandermann, Conversion of chloromethane over metal-exchanged ZSM-5 to higher hydrocarbons, Appl. Catal. 75 (1991) 133–152, https://doi.org/10.1016/S0166-9834(00)83129-2.
[32] Y. Sun, S.M. Campbell, J.H. Lunsford, G.E. Lewis, D. Palke, L.M. Tau, The catalytic conversion of methyl chloride to ethylene and propylene over phosphorus-modified Mg-ZSM-5 zeolites, J. Catal. 143 (1993) 32–44, https://doi.org/10.1006/jcat.1993.1251.
[33] Y. Wei, Y. He, D. Zhang, L. Xu, S. Meng, Z. Liu, B.L. Su, Study of Mn incorporation into SAPO framework: synthesis, characterization and catalysis in chloromethane conversion to light olefins, Microporous Mesoporous Mater. 90 (2006) 188–197, https://doi.org/10.1016/j.micromeso.2005.10.042.
[34] Y. Wei, D. Zhang, L. Xu, F. Chang, Y. He, S. Meng, B.L. Su, Z. Liu, Synthesis, characterization and catalytic performance of metal-incorporated SAPO-34 for chloromethane transformation to light olefins, Catal. Today 131 (2008) 262–269, https://doi.org/10.1016/j.cattod.2007.10.055.
[35] D. Zhang, Y. Wei, L. Xu, F. Chang, Z. Liu, S. Meng, B.L. Su, Z. Liu, MgAPSO-34 molecular sieves with various Mg stoichiometries: synthesis, characterization and catalytic behavior in the direct transformation of chloromethane into light olefins, Microporous Mesoporous Mater. 116 (2008) 684–692, https://doi.org/10.1016/j.micromeso.2008.06.001.
[36] J. Huang, W. Wang, Z. Fei, Q. Liu, X. Chen, Z. Zhang, J. Tang, M. Cui, X. Qiao, Enhanced light olefin production in chloromethane coupling over Mg/Ca modified durable HZSM-5 catalyst, Ind. Eng. Chem. Res. 58 (2019) 5131–5139, https://doi.org/10.1021/acs.iecr.8b05544.
[37] D. Zhu, Z. Wang, F. Meng, B. Zhao, S. Kanitkar, Y. Tang, Catalytic conversion of chloromethane to olefins and aromatics over zeolite catalysts, Catal. Lett. 151 (2021) 1038–1048, https://doi.org/10.1007/s10562-020-03364-z.
[38] J. Pérez-Ramírez, C. Mondelli, T. Schmidt, O.F.K. Schlüter, A. Wolf, L. Mleczko, T. Dreier, Sustainable chlorine recycling via catalysed HCl oxidation: from fundamentals to implementation, Energy Environ. Sci. 4 (2011) 4786–4799, https://doi.org/10.1039/C1EE02190G.
[39] C. Li, Y. Sun, I. Djerdj, P. Voepel, C.C. Sack, T. Weller, R. Ellinghaus, J. Sann, Y. Guo, B.M. Smarsly, H. Over, Shape-controlled $CeO_2$ nanoparticles: stability and activity in the catalyzed HCl oxidation reaction, ACS Catal. 7 (2017) 6453–6463, https://doi.org/10.1021/acscatal.7b01618.
[40] R. Martínez-Franco, Z. Li, J. Martínez-Triguero, M. Moliner, A. Corma, Improving the catalytic performance of SAPO-18 for the methanol-to-olefins (MTO) reaction by controlling the Si distribution and crystal size, Catal. Sci. Technol. 6 (2016) 2796–2806, https://doi.org/10.1039/C5CY02298C.
[41] Y. Wang, S.L. Chen, Y.J. Jiang, Y.Q. Cao, F. Chen, W.K. Chang, Y.L. Gao, Influence of template content on selective synthesis of SAPO-18, SAPO-18/34 intergrowth and SAPO-34 molecular sieves used for methanol-to-olefins process, RSC Adv. 6 (2016) 104985–104994, https://doi.org/10.1039/C6RA23048B.
[42] I.M. Dahl, S. Kolboe, On the reaction mechanism for propene formation in the MTO reaction over SAPO-34, Catal. Lett. 20 (1993) 329–336, https://doi.org/10.1007/BF00769305.
[43] I.M. Dahl, S. Kolboe, On the reaction mechanism for hydrocarbon formation from methanol over SAPO-34: 2. isotopic labeling studies of the co-reaction of propene and methanol, J. Catal. 161 (1996) 304–309, https://doi.org/10.1006/jcat.1996.0188.
[44] S. Wang, Y. Chen, Z. Qin, T.S. Zhao, S. Fan, M. Dong, J. Li, W. Fan, J. Wang, Origin and evolution of the initial hydrocarbon pool intermediates in the transition period for the conversion of methanol to olefins over H-ZSM-5 zeolite, J. Catal. 369 (2019) 382–395, https://doi.org/10.1016/j.jcat.2018.11.018.
[45] B.T.W. Lo, L. Ye, G.G.Z. Chang, K. Purchase, S. Day, C.C. Tang, D. Mei, S.C. E. Tsang, Dynamic modification of pore opening of SAPO-34 by adsorbed surface methoxy species during induction of catalytic methanol-to-olefins reactions, Appl. Catal. B 237 (2018) 245–250, https://doi.org/10.1016/j.apcatb.2018.05.090.
[46] Z. Zhu, W. Li, H. Zhang, T. Qin, D. Han, F. Wang, J. Zhang, G. Wang, L. Bing, One-pot synthesis of metal-containing SSZ-13 nanocrystals by interzeolite transformation of spent FCC catalysts for the methanol-to-olefins reaction, Appl. Catal. B 365 (2025) 124900, https://doi.org/10.1016/j.apcatb.2024.124900.
[47] Q. Liu, D. Wen, Y. Yang, Z. Fei, Z. Zhang, X. Chen, J. Tang, M. Cui, X. Qiao, Enhanced catalytic performance for light-olefins production from chloromethane over hierarchical porous ZSM-5 zeolite synthesized by a growth-inhibition strategy, Appl. Surf. Sci. 435 (2018) 945–952, https://doi.org/10.1016/j.apsusc.2017.11.153.
[48] P. Wang, L. Chen, J. Xie, H. Li, C.T. Au, S.F. Yin, Enhanced catalytic performance in $CH_3Br$ conversion to benzene, toluene, and xylene over steamed HZSM-5 zeolites, Catal. Sci. Technol. 7 (2017) 2559–2565, https://doi.org/10.1039/C7CY00334J.
[49] U. Olsbye, O.V. Saure, N.B. Muddada, S. Bordiga, C. Lamberti, M.H. Nilsen, K. P. Lillerud, S. Svelle, Methane conversion to light olefins—how does the methyl halide route differ from the methanol to olefins (MTO) route? Catal. Today 171 (2011) 211–220, https://doi.org/10.1016/j.cattod.2011.04.020.
[50] J. Valecillos, H. Manzano, A.T. Aguayo, J. Bilbao, P. Castaño, Kinetic and deactivation differences among methanol, dimethyl ether and chloromethane as stock for hydrocarbons, ChemCatChem 11 (2019) 5444–5456, https://doi.org/10.1002/cctc.201901204.
[51] B.V. L'vov, Mechanism of thermal decomposition of alkaline-earth carbonates, Thermochim. Acta. 303 (1997) 161–170, https://doi.org/10.1016/S0040-6031(97)00261-X.
[52] M. Bjørgen, S. Svelle, F. Joensen, J. Nerlov, S. Kolboe, F. Bonino, L. Palumbo, S. Bordiga, U. Olsbye, Conversion of methanol to hydrocarbons over zeolite H-ZSM-5: on the origin of the olefinic species, J. Catal. 249 (2007) 195–207, https://doi.org/10.1016/j.jcat.2007.04.006.
[53] T. Xu, Q. Zhang, H. Song, Y. Wang, Fluoride-treated H-ZSM-5 as a highly selective and stable catalyst for the production of propylene from methyl halides, J. Catal. 295 (2012) 232–241, https://doi.org/10.1016/j.jcat.2012.08.014.
[54] M. Westgård Erichsen, S. Svelle, U. Olsbye, H-SAPO-5 as methanol-to-olefins (MTO) model catalyst: towards elucidating the effects of acid strength, J. Catal. 298 (2013) 94–101, https://doi.org/10.1016/j.jcat.2012.11.004.
[55] M. Westgård Erichsen, S. Svelle, U. Olsbye, The influence of catalyst acid strength on the methanol to hydrocarbons (MTH) reaction, Catal. Today 215 (2013) 216–223, https://doi.org/10.1016/j.cattod.2013.03.017.

[56] X. Fang, F. Wen, X. Ding, H. Liu, Z. Chen, Z. Liu, H. Liu, W. Zhu, Z. Liu, Highly selective carbonylation of $CH_3Cl$ to acetic acid catalyzed by pyridine-treated MOR zeolite, Angew. Chem. Int. Ed. 61 (2022) e202203859, https://doi.org/10.1002/anie.202203859.
[57] X. Fang, B. Li, H. Liu, M. Xie, Z. Chen, L. Yang, J. Han, W. Zhu, Z. Liu, High carbon utilization for $CO_2$ conversion with chloromethane to aromatics over acidic zeolite catalyst, Chem. Catal. 3 (2023) 100689, https://doi.org/10.1016/j.checat.2023.100689.
[58] B. Li, X. Fang, H. Liu, Z. Chen, M. Xie, L. Yang, W. Zhu, Highly efficient production of aromatics from $C_2H_5Cl$ coupling with CO over H-zeolites, Catal Sci. Technol. 14 (2024) 878–884, https://doi.org/10.1039/D3CY01550E.
[59] M.D. Driessen, V.H. Grassian, Spectroscopic evidence for methyl spillover on silica-supported copper catalysts, Langmuir 11 (1995) 4213–4216, https://doi.org/10.1021/la00011a009.
[60] M.D. Driessen, V.H. Grassian, Methyl spillover on silica-supported copper catalysts from the dissociative adsorption of methyl halides, J. Catal. 161 (1996) 810–818, https://doi.org/10.1006/jcat.1996.0244.